Facet exposure-dependent photoelectrocatalytic oxidation kinetics of bisphenol A on nanocrystalline {001} TiO$_2$/carbon aerogel electrode

Ya-nan Zhang [a], Ning Qin [a], Jianyun Li [a], Shengnan Han [a], Pan Li [b], Guohua Zhao [a,*]

[a] School of Chemical Science and Engineering, Shanghai Key Lab of Chemical Assessment and Sustainability, Key Laboratory of Yangtze River Water Environment, Tongji University, 1239 Siping Road, Shanghai, China
[b] College of Environmental Science and Engineering, Tongji University, 1239 Siping Road, Shanghai, China

ABSTRACT

An anatase TiO$_2$ with {001} facet exhibits high oxidation activity towards the degradation of wastewater. The impact of {001} facet exposure degree on the degradation oxidation kinetics and mechanism is still unclear and urgently needs to be discussed. The photoelectrocatalytic (PEC) degradation of bisphenol A (BPA) in wastewater using facet-controlled nanocrystalline {001} TiO$_2$/carbon aerogel (CA) photo-electrodes was then investigated in this study. Nano-sized anatase {001} TiO$_2$ crystals with different {001} facet exposure degrees of high (90%), medium (48%) and low (15%) were constructed on a CA substrate via electrophoretic deposition. A positive correlation was found between the {001} facet exposure and the photocurrent density, electron carrier concentration and the total amount of •OH. Nearly 100% BPA removal efficiency was shown on the 90%-{001}TiO$_2$/CA in 6 h. The rate constant (k) value was 0.454 h^{-1} and the TOC rate was 83%. They are 1.8 and 1.8 times greater than those obtained on the 48%-{001}TiO$_2$/CA, as well as 3.5 and 2.4 times greater than those on the 15%-{001}TiO$_2$/CA, respectively. The greatly promoted PEC oxidation activity of 90%-{001}TiO$_2$/CA is due to its more rapidly accumulated intermediates products than other two photoelectrodes, which then completely mineralize into CO$_2$ and H$_2$O. This is mainly because of the highest oxidation sites existed on the 90%-{001}TiO$_2$ surface and the efficient separation of electron-hole pairs between the {001} TiO$_2$ and CA under the electric fields.

© 2017 Elsevier B.V. All rights reserved.

1. Introduction

Bisphenol A (BPA) is a known representative one of EDCs, has received great attention due to its biological toxicity and estrogenic activity [1]. The widespread application of BPA has resulted in its ubiquitous occurrence in landfill leachates, air, dust and industrial wastewaters, leading to the severe environmental problems [2]. Over the past decades, great efforts have been devoted to efficiently removing this emergent environmental pollutant. Since the conventional physical method and biological treatment are inefficient for the complete mineralization of the target organic pollutants [3,4], various other methods have been developed to remove BPA in wastewaters, such as the electrochemical oxidation [5], photo-catalytic method [6–11], and so on.

Among them, the photoelectrocatalytic (PEC) oxidation method, especially based on the TiO$_2$ materials, has been recognized as a highly efficient approach in mineralization and environmentally-sustainable treatment of the environmental pollutants [12]. Since the heterogeneous PEC is a surface-mediated advanced oxidation process in the solution, the interfacial chemistry will significantly influence the mass transfer of target pollutants, photonic efficiency and interfacial reactive rate [6]. Therefore, in order to enhance the PEC efficiency, it is extremely important to optimize the interface activity of TiO$_2$, for example, through TiO$_2$ crystal-facet tailoring [13–17]. The anatase TiO$_2$ crystals with exposed clean {001} crystal facet ({001}TiO$_2$) has been widely reported [18–20] and is believed to provide oxidation sites on the {001} facet, which possesses 100% five-fold coordinated Ti (Ti$_{5c}$) with the high surface energy of 0.90 J m^{-2} [13]. However, most of the reported {001}TiO$_2$ materials reported are in form of powder, which limited their application in photoelectrocatalysis (PEC). Previously, we have produced a nanocrystalline {001} TiO$_2$/carbon aerogel electrode by loading the nano-sized (50 nm) anatase {001} TiO$_2$ on a carbon aerogel (CA) substrate. Such an electrode provides improved separation efficiency between the holes and electrons under the effect of electric field [21]. The growth of nano-sized {001} TiO$_2$ in the porous network of CA was confirmed to be pretty easy as well. However, only 40% exposed {001} facet were obtained on the single nano-sized

{001} TiO_2 particle, which is probably restricted by the geometry and definite growing orientation.

In the context, we propose a more effective approach to construct a photoelectrode with high-percentage exposure of nano-sized TiO_2{001} facets, eventrually to acquire the superior PEC oxidation towards BPA in wasterwater. In this work, {001}TiO_2/CA photoelectrodes were constructed by deposition of the nano-sized TiO_2 crystal on the high surface-area CA substrate. An electrophoretic deposition (EPD) method was applied. The percentage of exposed {001} facet was accurately controlled by controlling the experimental conditions. The impact of {001} facet exposure on PEC oxidation activity of BPA was deeply analyzed by comparing the BPA removal, rate constant (k) value and generated intermediates products obtained on different x%-{001}TiO_2/CA photoelectrodes (x is denoted for the exposure percentage of the TiO_2{001} facets). The obtained PEC activity towards the degradation of BPA followed the order of 90%-{001}TiO_2/CA > 48%-{001} TiO_2/CA > 15%-{001} TiO_2/CA. The generated intermediates products during PEC processes, which were determined by high-performance liquid chromatography (HPLC) and liquid chromatography–mass spectrometry (LC–MS), were more rapidly accumulated and completely mineralized on the 90%-{001}TiO_2/CA. The photocatalytic and electrochemical characterization reveals a positive correlation between the facet exposure and the photocurrent density, electron carrier concentration, as well as the total amount of •OH radicals. The 90%-{001}TiO_2/CA generated the highest total amount of •OH in the course of PEC processes. The facets exposure-dependent degradation kinetics and possible mechanism were further discussed. The highest PEC oxidation activity towards the BPA removal on the 90%-{001}TiO_2/CA is mainly attributed to the following aspects. Firstly, the 90%-{001} TiO_2 with the highest exposed {001} surface area possesses the highest photocurrent density and generates the highest amount of •OH radicals, while the {001} facets act as oxidation sites with the presence of 100% Ti_{5c} atoms. Secondly, the near-perfect cube-shaped 90%-{001} TiO_2 is more easily to be grown in the porous network of CA, leading the efficient separation of electron-hole pairs between {001} TiO_2 and CA under the electric fields. The facets exposure-dependent degradation kinetics and possible mechanism were further explored. This study provides new insights and valuable original data with respect to the design of high efficiency TiO_2-facet based photoelectrode and its further environmental PEC applicability in the environmental fields.

2. Experimental

2.1. Reagents and materials

Sodium carbonate, sodium hydroxide, acetone, hydrofluoric acid (HF, ≥40 wt%), Ethyl alcohol, Benzoic Acid, Bisphenol A(AR) and sodium sulfate were purchased from Sinopharm (Shanghai, China). Tetrabutyl titanate (Ti(OC$_4$H$_9$)), Iodine, Methanol, Hydrogen Peroxide, Oleic acid, Oleylamine were obtained from Aladdin Co., China. 5,5-dimethylpyrroline–1–oxide (DMPO) was purchased from Sigma–Aldrich. All reagents were used directly and without further purification.

2.2. Synthesis of {001}TiO$_2$/CA

The {001}TiO_2 anatase crystals with different percentages of {001}facets were synthesized by carefully controlling the experiment parameters. In a typical hydrothermal synthesis [21], 0.6 mL of HF solution was slowly dropped into 5 mL Ti(OBu)$_4$. The obtained mixture was then put into a 50 mL Teflon-lined stainless steel autoclave and kept at 180 °C for 24 h. After a hydrothermal reaction,

the precipitates were collected. To remove the absorbed fluorine species, they were washed with 0.1 M NaOH aqueous solution. After drying at 80 °C in vacuum oven overnight, the 90%-{001}TiO_2 was finally harvested. In the case of 48%-{001}TiO_2, 0.25 mL of HF solution was dropwisely added into 5 mL Ti(OBu)$_4$, then 6 mL H$_2$O$_2$ solution was slowly added into the mixture. With other identified conditions, the obtained mixture was kept at 200 °C for 24 h. For the preparation of the 15%-{001}TiO_2, 1.4 mL of Ti(OBu)$_4$ was added to a mixture of 5.0 mL oleic acid, 9.1 mL oleylamine and 4.6 mL absolute ethanol. The obtained mixture was stirred for 10 min and then transferred into the Teflon-lined stainless steel autoclave, which contained 20 mL mixture of ethanol and water (96% ethanol, v/v). After heating the obtained product at 180 °C for 18 h, washing thoroughly with ethanol and water, and being dried at 80 °C in vacuum for overnight, the 15%-{001}TiO_2 were obtained [22].

Fabrication of {001}TiO_2 photoelectrode: First, 40 mg {001}TiO_2 nanoparticles and 10 mg iodine were dispersed in 50 mL acetylacetone. The obtained TiO_2 suspension was sonicated for 5 min before the application of a cathodic electrophoretic deposition (EPD) process [23]. CA was used as the cathodic substrate and a titanium plate served as the counter-electrode. The electrodes were inset into the 50 mL suspension with a distance of 2 cm. A constant voltage mode was applied during the EPD process. The bias voltage was 10 V at room temperature. The deposition time for the preparation of the 90%-{001}TiO_2, 48%-{001}TiO_2 and 15%-{001}TiO_2 during EPD process were 60, 30, and 15 min, respectively.,The loading amounts of TiO_2 were 12 mg/cm^2. After being dried at 60 °C in vacuum for 12 h, the {001}TiO_2/CA photoelectrodes were obtained.

2.3. Characterization

The morphology and microstructures of three {001} TiO_2 samples were characterized with scanning electron microscopy (SEM, Hitachi–S4800) and transmission electron microscopy (TEM, JEM-2100, JEOL). The X–ray diffraction (XRD) measurements were conducted on a Rigaku–D/max2550 powder diffractometer with Cu Kα radiation (40 kV, 30 mA over the 2θ range, 20–80 °C). X-ray photoelectron spectroscopy was carried out on a Kratos ASIS-HS X-ray photoelectron spectroscope equipped with a standard and monochromatic source (Al Kα) and operated at 150W (15 kV, 10 mA). Raman spectra were recorded on a Raman spectrometer (Renishaw Crop., UK) using a He/Ne laser with the wavelength of 515 nm. Electron spin resonance (ESR) spectra were obtained on a Bruker EMX Xplus–10/12 with a Microwave Bridge (a microwave frequencyof 9.853 GHz; a microwave powerof 20 mW; a modulation amplitude of 1 G; a modulation frequency of 100 kHz). Electron paramagnetic resonance (EPR) signals were measured using a Bruker, EMX plus-10/12 with a Microwave Bridge (microwave frequency, 9.853 GHz; microwave power, 20 mW; modulation amplitude, 1 G; modulation frequency, 100 kHz). To create DMPO-•OH adducts, {001}TiO_2 was mixed with 5, 5-dimethypylpyrroline-1-oxide (DMPO) and 30 s of photoirradiation was applied with 50 μL of the sample collected from the suspension photocatalysis system.

2.4. Photoelectrochemical measurement

PEC experiments were performed on a CHI660C electrochemical workstation using a conventional three-electrode, where the prepared {001} TiO_2 loaded on the FTO was as the working electrode, a saturated calomel electrode (SCE) as the reference electrode and a platinum foil as the counter electrode. A 150W LA-410UV-3 lamp (Hayashi, Japan) was used as the visible-light source. Its wavelength was in the range of 420–800 nm. The amperometric i-t method was utilized to monitor the PEC current in 0.1 mol/L Na$_2$SO$_4$ solution. A
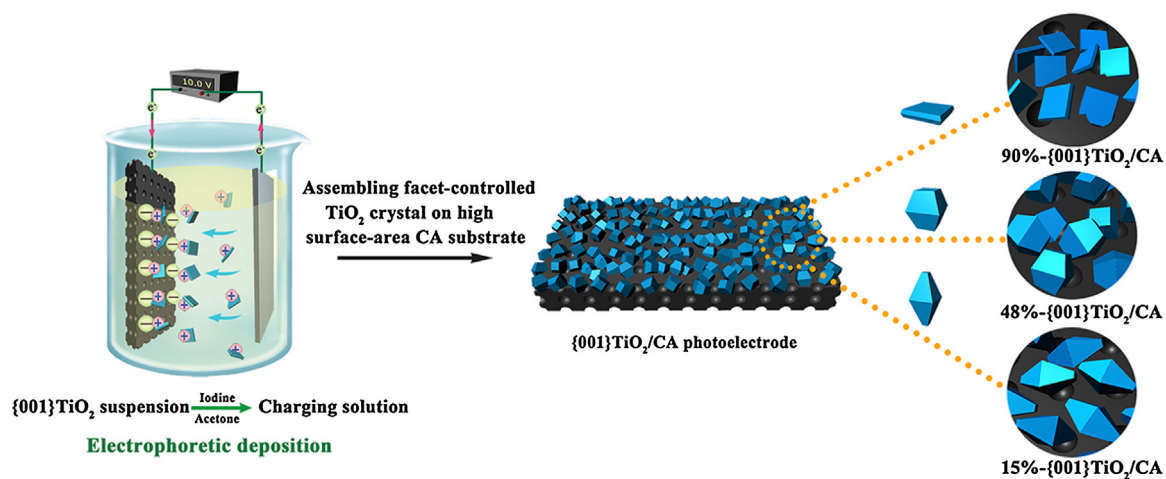
Scheme 1. Schematic plots of the photoelectrodes' fabrication.
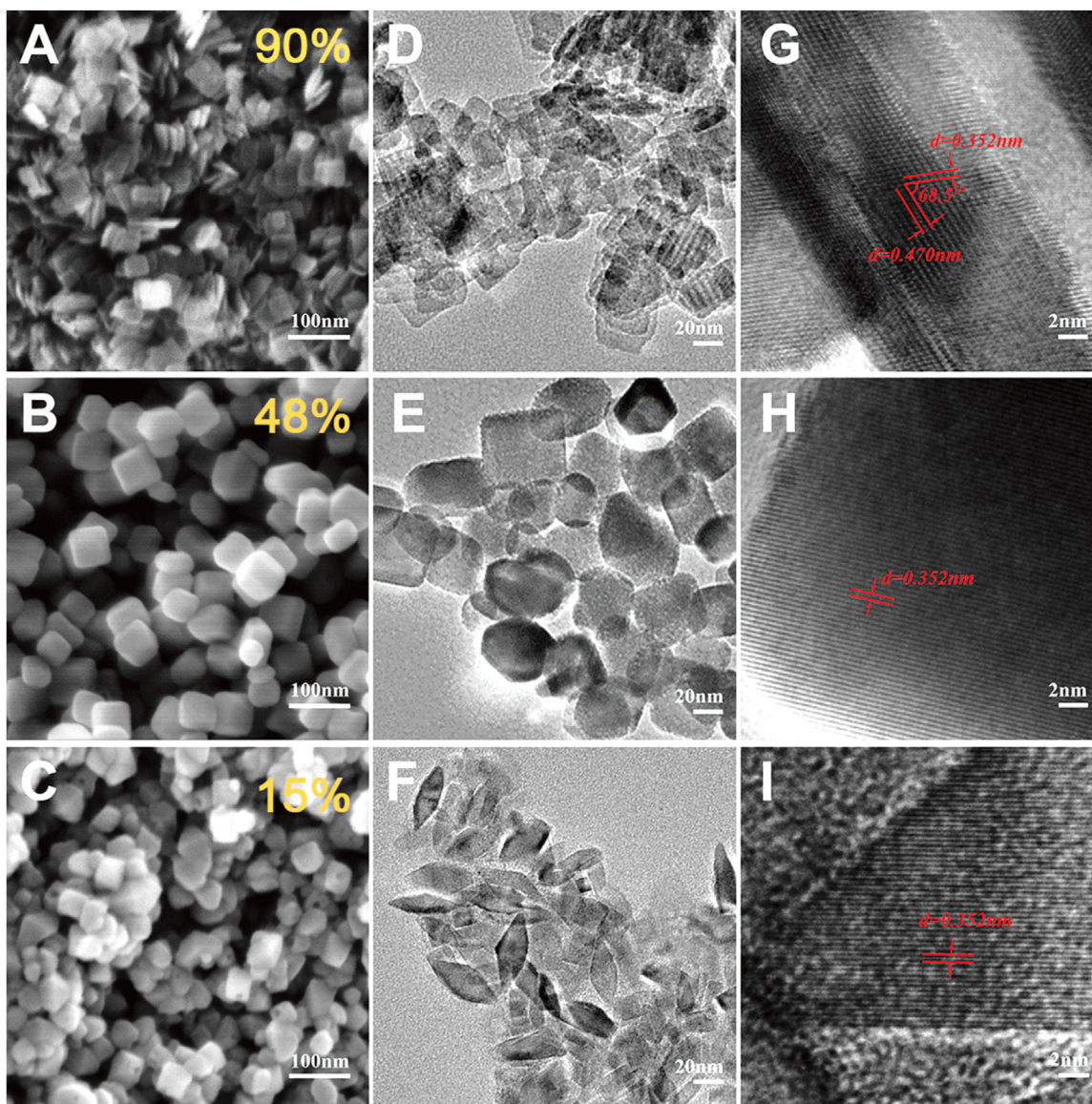
Fig. 1. SEM (A–C), TEM (D–F), and corresponding SAED patterns (G–I) of 90%-{001} TiO$_2$/CA (A,D,G), 48%-{001} TiO$_2$/CA (B,E,H), and 15%-{001} TiO$_2$/CA (C,F,I), respectively.
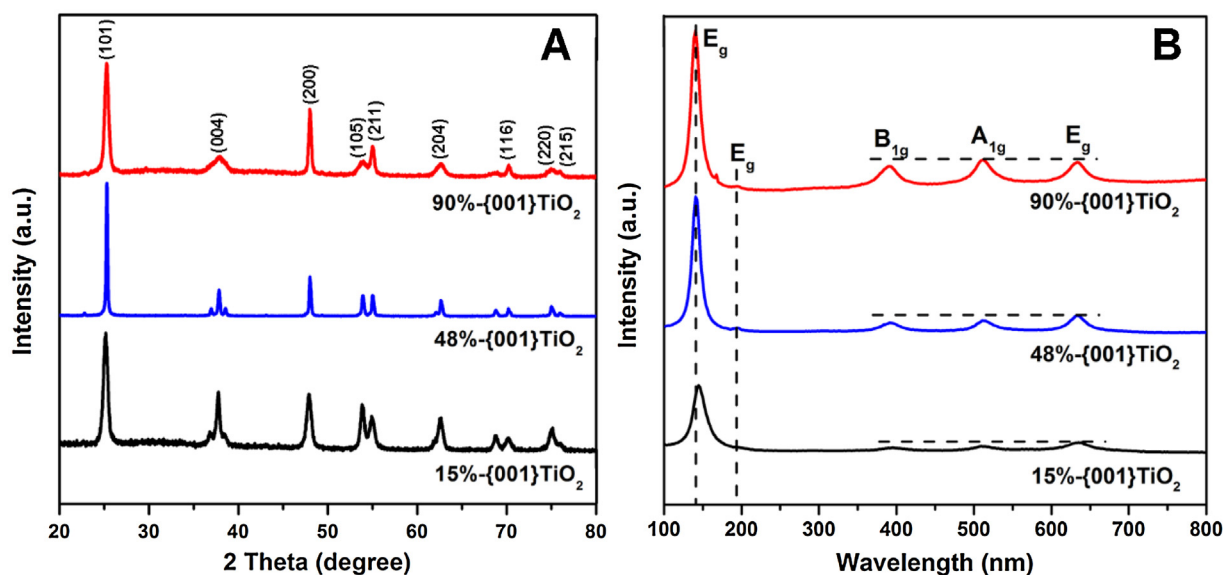
Fig. 2. XRD patterns (A) and Raman spectra (B) of three kinds of {001} TiO$_2$ samples.

constant potential of 0.9 V (vs. SCE) was applied and the distance of the working electrode from the light center was kept as 1 cm.

2.5. Degradation experiment and analysis of degraded samples

The PEC oxidation of BPA was carried out in a quartz tubular reactor with a magnetic stirrer. The temperature was kept at a constant temperature (25 °C) with a jacketed cooler. A 300 W Xe high-pressure short-arc xenon lamp (PLS-SXE300, PerfectLight Technology Co. Ltd., Beijing, China) was used as the light source. The 100 mL BPA of 10 mg/L was degraded at a bias of + 0.9 V (vs SCE) under AM 1.5 irradiation (100 mW cm^{-2}). The concentration of BPA during the degradation was measured by high-performance liquid chromatography a HPLC (Agilent 1260) with AQ-C18 (4.6 mm × 100 mm, 5 μm) and a selected UV detector at λ = 276 nm. A 40:60 (v/v) methanol/water mixture was used as the mobile phase at the flow rate of 0.8 mL/min. The quantitation of •OH was determined with the reported method which was reported in the previous literature [24]. The total organic carbon (TOC) values were determined by a Multi 3100 TOC/TN analyzer. The identification of degradation intermediates of BPA was carried out on a liquid chromatography–mass spectrometry instrument (LC–MS). The LC system with a capillary column (Agilent C18, 150 mm × 4.6 mm, 5 μm) was interfaced to a Varian310 triple quadrupole MS via electrospray ionization (ESI) source. The ESI was operated in a negative ionization (PI) mode with high purity nitrogen gas. The parameters were setted as followings: a capillary voltage of 3.5 kV, a gas temperature of 350 °C, a drying gas flow rate of 7 dm^3/min. Mass spectra were acquired over an m/z range of 100–400.

3. Results and discussion

3.1. Facet exposure-controlled growth of {001} TiO$_2$ on high surface-area CA

An EPD method was employed in our work to prepare the {001} TiO$_2$/CA photoelectrodes. The procedure is schematically shown in Scheme 1. When the TiO$_2$ particles are suspended in a "charging solution" that contains the small additives of iodine, acetone and water, the H$^+$ ions generated in solution will be adsorbed on the particles surface to form "charged TiO$_2$ particles" [25]. These charged TiO$_2$ nanoparticles are migrated towards the oppositely

charged cathode when an EC electric field is applied, leading to the deposition of TiO$_2$ nanoparticles on the CA substrate. The loading amount of {001} TiO$_2$ is possible to be precisely controlled by conveniently varying the deposition voltage and time. It has to point out that the applied deposition time for preparing the 90%-{001}TiO$_2$, 48%-{001}TiO$_2$ and 15%-{001}TiO$_2$ were 60, 30 and 15 min, respectively, while the loading amount was almost same (12 mg cm^{-2}). Compared with the formation of 90%-{001}TiO$_2$, the fabrication of 15%-{001}TiO$_2$ with the larger percentage of {101} facet was easily and quicker when the generated H$^+$ ions are more inclined to adsorb on the reduction site of {101} facet.

The SEM images of the {001}TiO$_2$/CA with different percentages of {001} facets are shown in Fig. 1. All of the {001} TiO$_2$ nanoparticles with the similar amount and size of 40–50 nm are well-dispersed on the surface of CA. As shown in Fig. 1C, a typical truncated bi-pyramid is observed when the percentage of {001} is only 15% (15%-{001} TiO$_2$). With an increase of the percentage of {001} facets, the length of bi-pyramid decreases whereas the truncated area increases gradually. When the percentage of {001} facet increases to 90% (90%-{001} TiO$_2$), the near-perfect cube-shaped {001} TiO$_2$ with thickness of 8 nm is obtained (Fig. 1A). The relative {001} facets percentages of individual TiO$_2$ samples have been calculated from the surface area of {101} and {001} facets [21,26]. These results are summarized in Table 1. The highest total surface area (S_{BET}) of 76.52 m^2/g obtained on the 90%-{001}TiO$_2$ provides the highest exposed {001} facets area ($S_{\{001\}BET}$) of 68.87 m^2/g, which play crucial roles in determining its photocatalytic activity [27]. Microscopic observation of each {001} TiO$_2$ nanoparticles was conducted via the high resolution transmission electron microscopy (HRTEM). Both Fig. 1E and F reveal that the measured lattice spacing of 0.351 nm for the prepared TiO$_2$ nanoparticles indicative of (101) planes of anatase TiO$_2$. A clear side view of TiO$_2$ nanosheet is shown in Fig. 1G. Two sets of lattices with fringe spacing of 0.352 and 0.474 nm are seen, corresponding to the (101) and (002) planes of anatase TiO$_2$, respectively [22]. The interfacial angle of 68.3° is consistent with the theoretical value of the angle between the {101} and {001} facets [28], further confirming that the cubic TiO$_2$ nanosheet are mainly enclosed by high-energy {001} facets.

Fig. 2A illustrates XRD patterns of the 90%-{001} TiO$_2$, 48%-{001} TiO$_2$, and 15%-{001} TiO$_2$. All samples showed peaks at 2θ values of 25.3°, 38.2°, and 48.1°, corresponding to the (101),

(004), and (200) crystal planes (JCPDS No. 21-1272) of anatase TiO_2 [28], respectively. Obviously, the full width at half-maximum of (004) diffraction peaks was found to be decreased gradually from 15%-{001} TiO_2 to 90%-{001} TiO_2. This suggests that the minimum thickness of the TiO_2 crystals in the [001] direction has been achieved on the 90%-{001} TiO_2, leading to the maximum percentage of {001} facets [29]. In the Raman spectra, (Fig. 2B), five strong vibration peaks appear at 149.1 cm^{-1} (Eg), 198.3 cm^{-1} (Eg), 391.1 cm^{-1} (B$_{1g}$), 503.7 cm^{-1} (A$_{1g}$) and 630.0 cm^{-1} (Eg). These peaks are typical characteristics of anatase TiO_2 phase [30]. Notice that the intensity of the Eg peaks decreases gradually along with the percentage of {001} increases, owing to the gradual decrease of symmetric stretching vibration modes of O−Ti−O. Meanwhile, the intensity of B$_{1g}$ and A$_{1g}$ peaks are the highest in the 90%-{001} TiO_2, which is mainly caused by the strong symmetric bending vibration and anti-symmetric bending vibration [31]. From the results obtained from XRD and Raman spectroscopy, we can state the successful construction of three different {001} TiO_2/CA photoelectrodes.

3.2. PEC degradation and oxidation kinetics of BPA on different facet-exposed {001}TiO_2/CA

Three {001}TiO_2/CA photoelectrodes were then applied in the PEC degradation of BPA. Fig. 3A shows the concentration ratios of BPA as a function of PEC reaction time. On three photoelectrodes, the degradation are rapid. The degradation rate follow the order of 15%-{001}TiO_2/CA < 48%-{001}TiO_2/CA < 90%-{001}TiO_2/CA. The BPA degradation removal ratio on the 15%-{001} TiO_2/CA is 55.6% after a reaction time of 6 h and on the 48%-{001}TiO_2/CA it is 76.7%. When the 90%-{001}TiO_2/CA is applied as the photoanode, the BPA degradation removal ratio reaches 99.6% only with a reaction time of 4 h.

The oxidation kinetics of BPA on these photoanodes was further studied. As shown in Fig. 3B, the degradation of BPA on three photoanodes follows pseudo-first order kinetics. The calculated rate constant (k) for BPA oxidation on the 48%-{001}TiO_2/CA and 15%-{001}TiO_2/CA is 0.255 and 0.130 h^{-1}, respectively. The k value of BPA obtained on the 90%-{001} TiO_2/CA is 0.454 h^{-1}, which is almost 1.8 and 3.5 times of that obtained on the 48%-{001}TiO_2/CA and 15%-{001} TiO_2/CA, respectively. The total organic carbon (TOC) was measured and the results are presented in Fig. 3C. The mineralization rate in the present of the 90%-{001}TiO_2/CA reaches 83% upon light irradiation for 6 h, while it is only 47% and 35% on the 48%-{001}TiO_2/CA and 15%-{001}TiO_2/CA, respectively. The 90%-{001} TiO_2/CA showes the highest degradation and mineralization capability for BPA. This result reveals that the PEC oxidation activity of these photoelectrodes is enhanced with an increase of exposed of {001} facet.

To better clarify the degradation kinetics of BPA oxidation on these photoanodes, the formed intermediate products during PEC processes were analyzed by LC–MS analysis [32]. Seven kinds of aromatic intermediates are detected during the PEC process on all photoelectrodes. The chemical structures and main mass fragmentation data of these intermidiates are listed in Table 2, including 4-isopropenylphenol, 1-(4-hydroxyphenyl) ethanone, PBA 3,4-quinone, BPA catechol, 4-(2-(3,4-dioxocyclohexa-1,5-dienyl) propan-2-yl) cyclohexa-3,5-diene-1,2-dione, (2Z,4E)-4-(formylmethylene)−5-methyl-5-(3,4-dioxocyclohexa-1,5-dienyl) hex-2-enoic acid and (1Z,5E,6Z)−5-(hydroxymethylene) −4,4-dimethylhepta-1,6-diene-1,3,7-tricarboxylic acid. A possible pathway for the BPA degradation on these photoanodes is then proposed in Fig. 4. Two possible sites are suggested for the attack of •OH radicals, producing different primary intermediates. They are named as route A and B. In route A, the •OH radicals attack the electron-rich

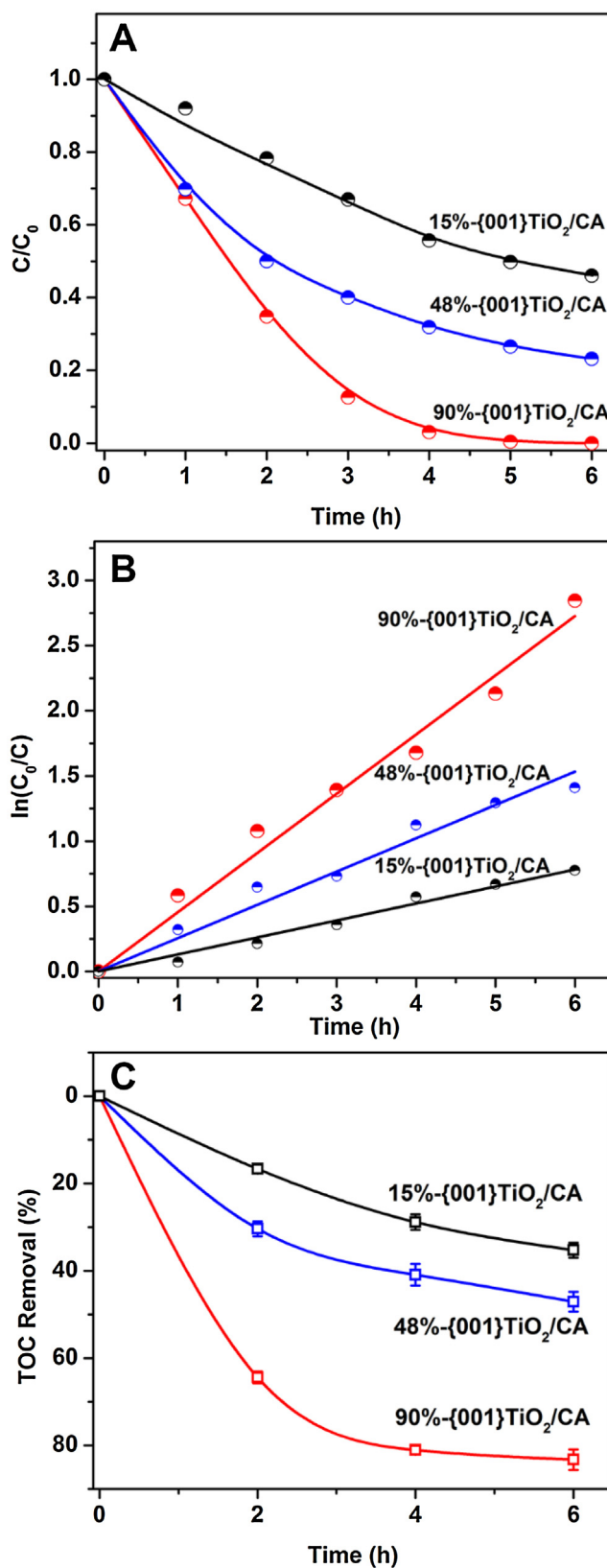Fig. 3. The PEC removal rate of BPA (A), kinetic analysis (B), and TOC removal rate (C) on the {001}TiO_2/CA photoelectrodes.

Table 1
Summary of characterization of the three kinds of {001}TiO$_2$ samples.

Sample	XRD crystal size (nm)	Exposed {001} facet (%)	TiO$_2$ loading amount (mg/cm^2)	S_{BET} (m^2/g)	$S_{\{001\}BET}$ (m^2/g)	Eg (eV)	Carrier density (10^{18} cm^{-3})
90%-{001}TiO$_2$	51.4	90	12.10	76.52	68.87	3.19	9.05
48%-{001}TiO$_2$	58.2	48	11.95	54.66	26.23	3.20	6.18
15%-{001}TiO$_2$	49.8	15	13.04	25.70	3.86	3.22	1.91

The percentage of {001} facet was approximately estimated by the following equation:
$S\{001\}_{exp} (\%) = S\{001\}/(S\{101\} + S\{001\}) = 2a/[4ab + 2a^2] \times 100$
where a and b correspond to the average side length and thickness of nanosheets by measuring more than 100 particles in TEM images.

Table 2
The major mass fragments (m/z) detected by means of LC/MS and the possible chemical structures of main intermediates during BPA PEC degradation on the {001}TiO$_2$/CA photoelectrodes.

No.	m/z	Moler Mass(g/mol)	Structural Formula	Molecular Formula
1	133	134		$C_9H_{10}O$
2	135	136		$C_9H_{12}O_2$
3	241	242		$C_{15}H_{14}O_3$
4	243	244		$C_{15}H_{16}O_3$
5	255	256		$C_{15}H_{12}O_4$
6	273	274		$C_{15}H_{14}O_5$
7	283	284		$C_{13}H_{16}O_7$
8	227	228		$C_{15}H_{16}O_2$

alkyl carbon, the 4-(2-hydroxypropan-2-yl) phenol (compound 1) is formed and convert to 4-isopropenylphenol (compound 2) and 1-(4-hydroxyphenyl) ethanone (compound 3) in sequence. They are presumably further oxidized through ring-rupturing reactions into CO$_2$ and H$_2$O. In route B, the •OH radicals attack the aromatic ring in the BPA, hydroxyl-BPA (compound 4) is produced, then converted to quinone-BPA (compound 5) and dihydroxylated-BPA (compound 6). Subsequently, the generated diquinone-BPA (compound 7) is followed by the formation of a series of aliphatic compounds, which contains carboxylic groups along with the cleavage of benzene rings (compound 8–10). All of the aromatic ring-opening products are further oxidized to produce carboxylic acid and eventually mineralized into CO$_2$ and H$_2$O during PEC processes.

The evolution of four typical intermediates products at different irradiation time intervals (0–4 h) were determined by HPLC and displayed in Fig. 5. Different accumulation-destruction cycles were observed on three photoelectrodes. For 90%-{001}TiO$_2$/CA (red lines), it is clear that the concentration of all the products are rapidly accumulated from the start and reached the maximum concentration (C_{max}) between 2 h and 3 h. Finally, the concentration of all products, especially the mono-benzene ring product (1-(4-hydroxyphenyl)ethanone), decreases completely after 4 h, suggesting a full mineralization. This explains well the observed efficient removal of TOC value on the 90%-{001}TiO$_2$/CA in Fig. 3C. In the case of the 48%-{001}TiO$_2$/CA (blue lines), the products are accumulated slower than those on the 90%-{001}TiO$_2$/CA and reached the C_{max} at a reaction time of 3 h. After 4 h, the most of BPA catechol and PBA 3,4-quinone were degraded (Fig. 5A and B), but concentration of the aromatic ring-opening products, such as the (1Z,5E,6Z)−5-(hydroxymethylene)−4,4-dimethylhepta−1,6-diene-1,3,7-tricarboxylic acid and 1-(4-hydroxyphenyl) ethanone (Fig. 5C and D) were still remained stable. In contrast, the products on the 15%-{001}TiO$_2$/CA are accumulated consistently during the irradiation even after 4 h. Compared with those on the 15%-{001} TiO$_2$/CA and 48%-{001}TiO$_2$/CA, the intermediates products generated in the course of a PEC process on the 90%-{001}TiO$_2$/CA are more rapidly accumulated and completely mineralized. The facts
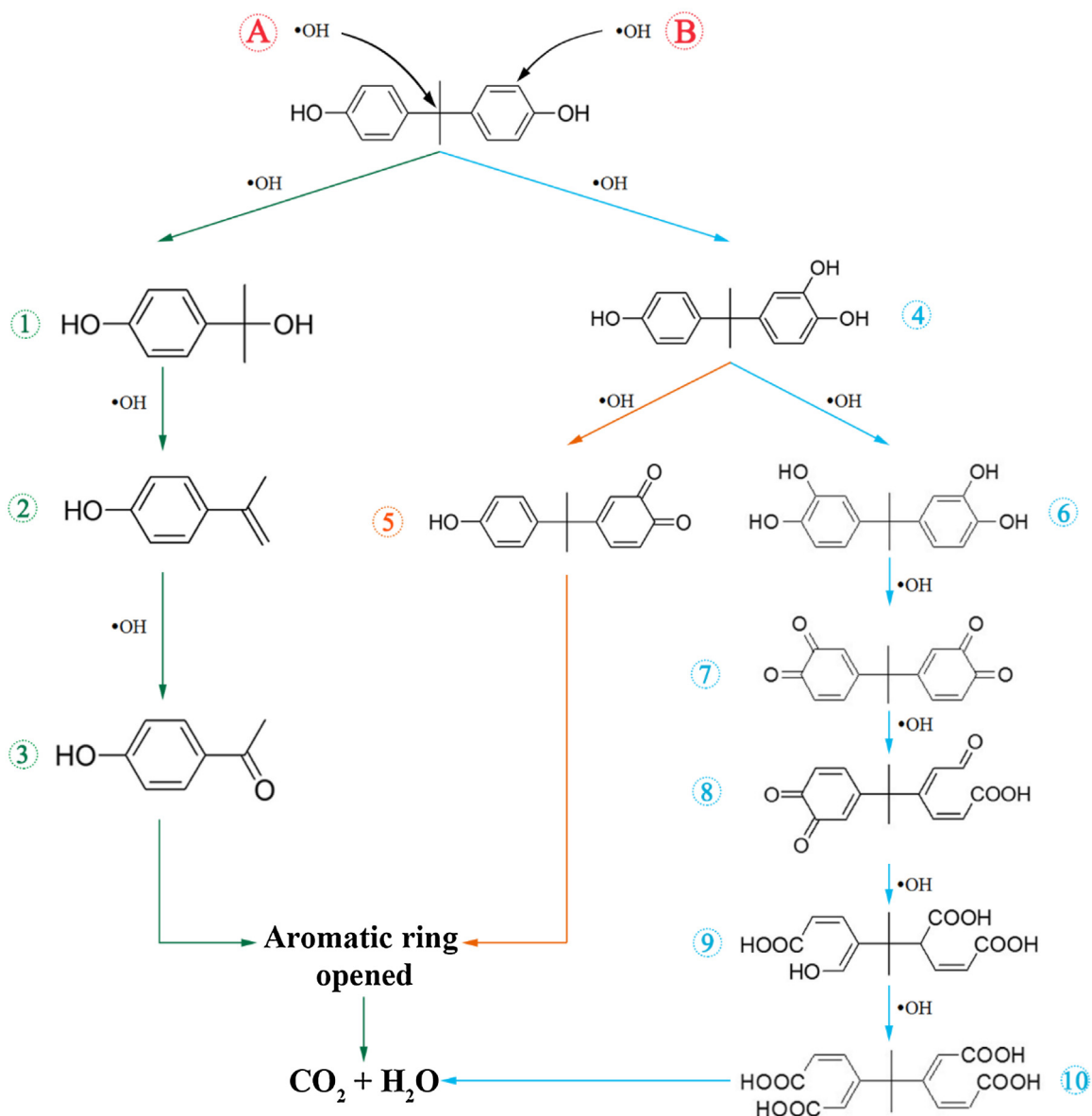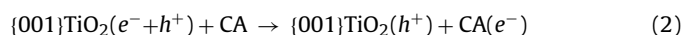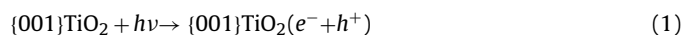
Fig. 4. Proposed reaction pathways of BPA degradation on three {001}TiO$_2$/CA photoelectrodes.

are in good consistent with the measured TOC values. Therefore, the 90%-{001}TiO$_2$/CA has the excellent PEC oxidation ability towards BPA. Otherwise, a comparison of the four intermediate formation at different conversion of BPA was further conducted on three photoelectrodes. As shown in Fig. S1, the change in concentration of four intermediate products on every photoelectrode is consistent with the BPA conversion.

3.3. Facet exposure-dependent PEC mechanism of {001}TiO$_2$/CA

Based on the above analysis, the PEC degradation of BPA on the over {001} TiO$_2$/CA photoelectrodes occurs as follows:

$$\{001\}TiO_2 + h\nu \rightarrow \{001\}TiO_2(e^- + h^+) \qquad (1)$$

$$\{001\}TiO_2(e^- + h^+) + CA \rightarrow \{001\}TiO_2(h^+) + CA(e^-) \qquad (2)$$

$$CA(e^-) + external\,electrostatic\,field \rightarrow external\,circuit \qquad (3)$$

$$h^+ + H_2O \rightarrow H^+ + {}^\bullet OH \qquad (4)$$

$${}^\bullet OH + h^+ + BPA \rightarrow degradation\,product \qquad (5)$$

When {001} TiO$_2$/CA is irradiated by simulated solar light, the photo-generated electrons on {001} TiO$_2$ are rapidly transferred to CA substrate and then to the external circuit under the electric field, leading the efficient separation of electron-hole pairs. The photo-generated holes will react with H$_2$O to generate hydroxyl radical ($^\bullet$OH), which are the major oxidative species for BPA degradation. Such a process is schematically shown in Scheme 2.

To find out the possible reasons for the different PEC oxidation ability of the three {001}TiO$_2$/CA photoelectrodes, the generated $^\bullet$OH involved in both photocatalytic and PEC process was studied by EPR spin-trap technique. The 5,5-dimethyl-1-pyrroline N-oxide (DMPO) as a nitrone spin trap was used for trapping the hydroxyl radical ($^\bullet$OH) [33]. In a photocatalytic process (Fig. 6A), the typical 4-fold characteristic peaks of DMPO-$^\bullet$OH adducts with an intensity ratio of 1:2:2:1 was be observed over the 15%-{001}TiO$_2$, 48%-{001}TiO$_2$, and 90%-{001}TiO$_2$ [34], elucidating that the $^\bullet$OH radicals are really generated on the {001}TiO$_2$ systems under light irradiation. The reactivity order of faceted {001}TiO$_2$/CA in generating $^\bullet$OH is then in the order of 90%-{001}TiO$_2$/CA > 48%-{001}TiO$_2$/CA > 15%-{001}TiO$_2$/CA.
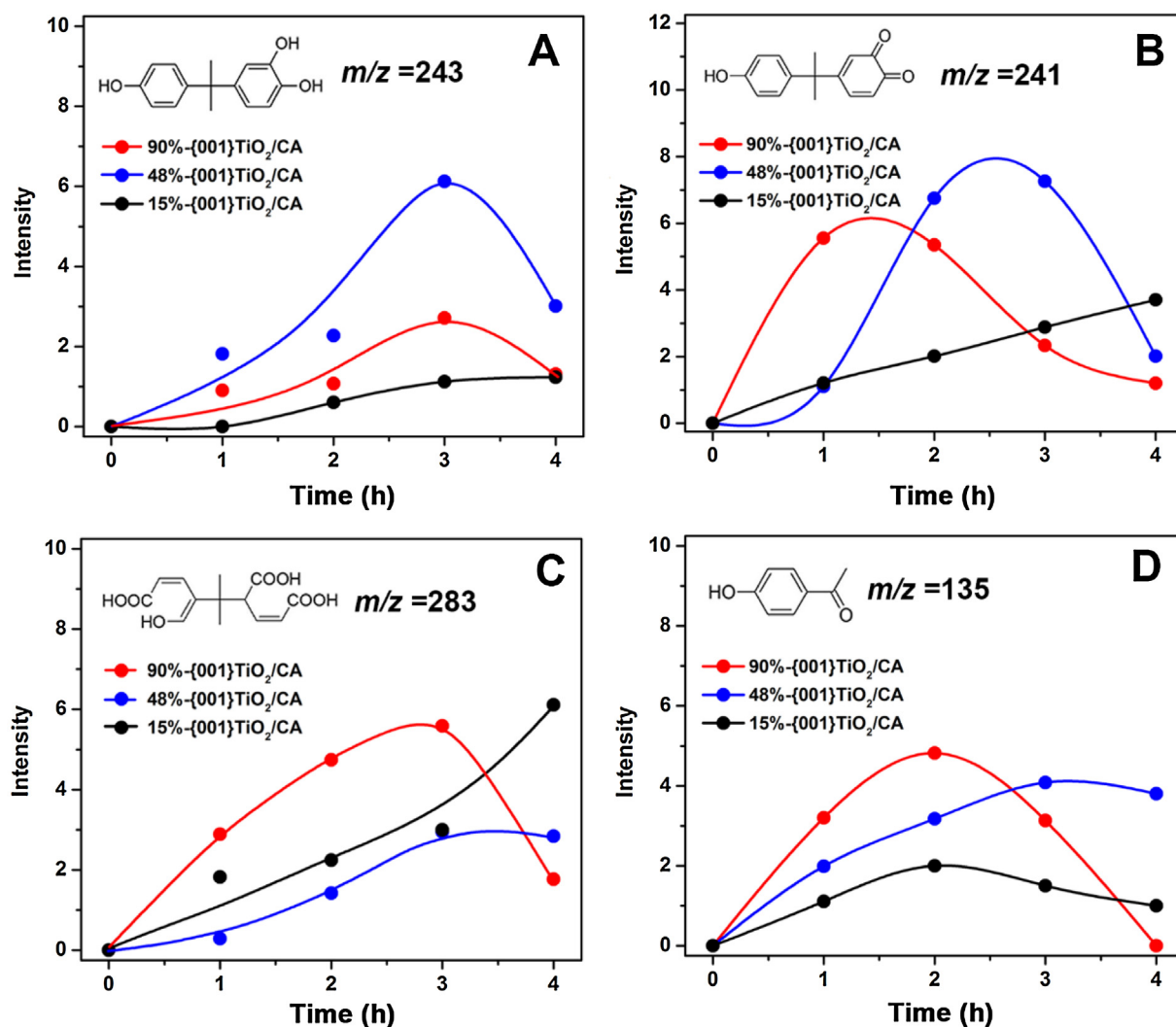
Fig. 5. Evolution of the generated intermediates during BPA PEC degradation as a function of irradiation times on the {001}TiO$_2$/CA photoelectrodes.
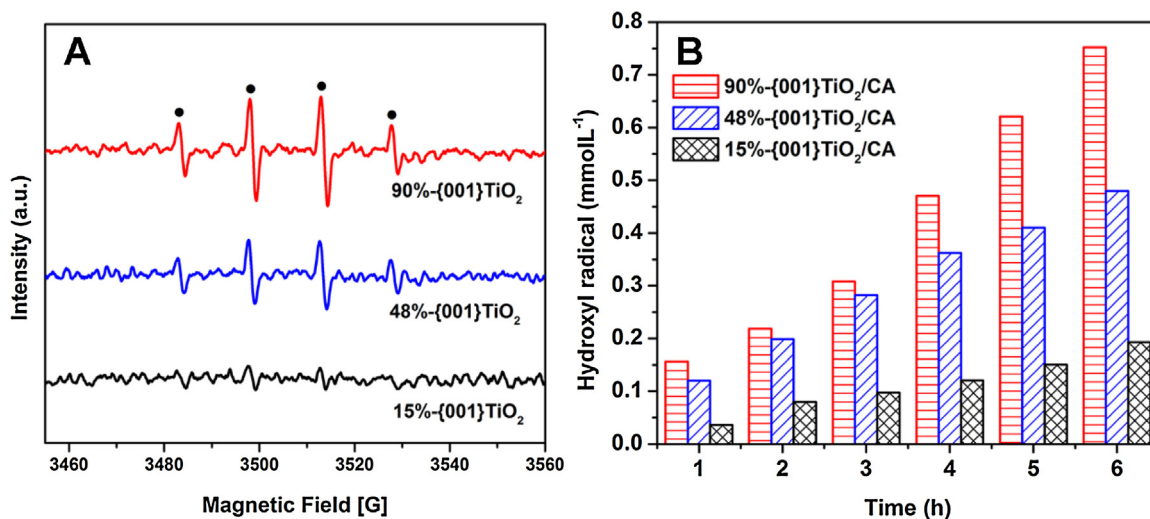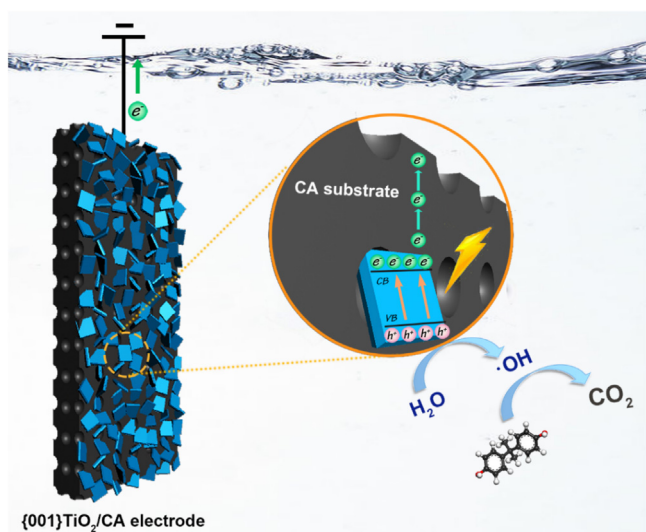

Fig. 6. EPR spectra of in-situ illuminated {001} TiO$_2$ samples in water (A) and the total concentrations of •OH formed as a function of illumination times (B) during BPA PEC degradation processes.

Scheme 2. Schematic illustration for PEC degradation of BPA on the (001)TiO_2/CA photoelectrodes.

Furthermore, the cumulative amount of •OH generated in PEC oxidation process was quantitatively determined by HPLC. Benzoic acid was utilized as a probe molecular (Fig. 6B). The reaction rate constant of benzoic acid reacting with •OH is $4.2 \times 10^9 \, M^{-1} \, s^{-1}$ in aqueous media [35]. In contrast to the photocatalytic process, the electric field applied in PEC process could enhance the charge separation efficiency and contribute most of the available holes for oxidation reactions, producing more larger amounts of •OH radicals on three photoelectrodes. This statement is supported by the results shown in Fig. 6B, where the amount of •OH obviously increases as a function of the irradiation times. For example, after 6 h, the amount of •OH radicals on the 90%-{001}TiO_2/CA reaches to $0.75 \, mM \, L^{-1}$, which is approximately 1.6 and 4.0 times of that ($0.48 \, mM \, L^{-1}$) on the 48%-{001}TiO_2/CA and that ($0.19 \, mM \, L^{-1}$) on the 15%-{001}TiO_2/CA. This agrees with that shown in Fig. 5A. All these facts indicate clearly a positive correlation between the facet exposure of {001}TiO_2 and the total amount •OH radicals. Therefore, the 90%-{001}TiO_2/CA owns the most efficient PEC degradation ability towards BPA degradation due to the highest concentration of •OH radicals on its surface.

To find out the effect of crystal facet exposure and additional bias potential on the PEC oxidation capability for BPA, the photocatalytic and electrochemical characterization of three photoelectrodes were further conducted. The UV/Vis DRS absorption spectra of the three photoelectrodes are shown in Fig. 7A. The absorption edge of 90%-{001}TiO_2 showes a slight red-shift from 385 nm to 389 nm, suggesting the widest absorption range. The plots of transformed Kubelka-Munk function versus the energy of light (inset of Fig. 7A) reveals that 90%-{001}TiO_2 has the smallest band gap of 3.19 eV in contrast to that of 48%-{001}TiO_2 and 15%-{001}TiO_2 with 3.20 and 3.22 eV, respectively [36]. The positive slopes of the linear parts of Mott-Schottky plots in Fig. 7 B confirm the n-type nature of three photoelectrodes. And the calculated falt-band potentials for the 90%-{001}TiO_2, 48%-{001} TiO_2 and 15%-{001}TiO_2 are −0.520 eV, −0.544 eV, and −0.564 eV, respectively. Consequently, the bottom of conduction band is located at 0.2 eV more negative than the flat band potential [37]. The valence band (VB) XPS spectra of (Fig. 7C) [38,39] shows that the high-energy shift of the VB edge (0.45 eV) is observed on the 90%-{001}TiO_2, different from those for the 48%-{001} TiO_2 and the15%-{001}TiO_2. The higher VB value of the 90%-{001}TiO_2 suggests the higher oxidation potential, which facilitates the production of •OH radicals [40]. In other words, the amount of formed •OH radicals follows

the same order as shown in Fig. 6. Otherwise, an additional peak at about 11.3 eV is observed on the 90%-{001}TiO_2. This indicates that the existence of oxygen vacancies is derived from the exposed {001} facets [41]. The substantial oxygen deficiency is attributed to the 100% Ti_{5c} of {001} facet, which accelerates obviously the transport mobility of charge carriers and prevents the recombination of electrons and holes. The possible electronic band structures of three {001}TiO_2 samples are summarized illustrated in Fig. 7D. The narrow band gap of the 90%-{001} TiO_2 produces the greatest amount of electrons and holes [40].

Using the following equation, the capacitance was further determined by calculating the carrier density (N_D) [42,43].

$$1/C_{sc}^2 = 2 \times (\Delta\Phi sc - RT/F)/(e\varepsilon_0\varepsilon N_D) \quad (6)$$

where Csc (F) is the capacitance of space charge region, $\Delta\Phi sc$ ($= V - V_{FB}$) is the potential difference of space charge region, V is the applied potential, V_{FB} is the flat band potential, R ($=8.314 \, J \, K^{-1} \, mol^{-1}$) is the gas constant, T is Kelvin temperature, F ($=96,485 \, C \, mol^{-1}$) is Faraday constant, with e ($= 1.602 \times 10^{-19} C$) is the electron charge, ε_0 is electric constant in vacumm ($= 8.854 \times 10^{-12} \, F/m$), and ε ($= 48 \, F/m$) is the electric constant for anatase TiO_2, and N_D is the carrier density ($1/cm^3$). As shown in Table 1, the calculated N_D of the 90%-{001}TiO_2 is $9.05 \times 10^{18}/cm^3$, which is nearly 1.4 times of that ($1.91 \times 10^{18}/cm^3$) obtained on the 48%-{001}TiO_2 and 5 times of that ($1.91 \times 10^{18}/cm^3$) on the 15%-{001}TiO_2, respectively. The largest N_D in the 90%-{001} TiO_2 indicates the highest separation efficiency of electrons and holes on this photoelectrode.

Fig. 8A presents the Nyquist plots of three photoelectrodes. The 90%-{001}TiO_2 shows the lowest resistance that is much smaller than that for the 48%-{001}TiO_2 and for the 15%-{001}TiO_2. This implies its smallest charge transfer resistance, its fastest electron mobility, namely the fastest reaction rate under the electric field.

Fig. 8B showes the amperometric current-time (i–t) curves of three photoelectrodes under the irradiation in 0.1 mol/L Na_2SO_4 with a bias voltage of 0.9 V. Comparatively, the largest photocurrent density of $2 \times 10^2 \, mA/cm^2$ is observed on the 90%-{001}TiO_2, which is 3.1 times of that ($0.65 \times 10^2 \, mA/cm^2$) on the 48%-{001} TiO_2 and 8.0 times of that ($0.25 \times 10^2 \, mA/cm^2$) on the 15%-{001}$TiO_2$, respectively. As mentioned above, the increase of S_{BET} for the 90%-{001}TiO_2 were only 1.4 and 3.0 times of that for the 48%-{001}TiO_2 and for the15%-{001}TiO_2, respectively. However, the increase of $S_{\{001\}BET}$ for the 90%-{001} TiO_2 is 1.9 and 6.0 times of 48%-{001}TiO_2 and 15%-{001}TiO_2. Therefore, the largest photocurrent density on the 90%-{001}TiO_2/CA photoelectrode is more ascribed to the increase of the exposed {001} facets, instead of its specific surface area.

Based on the above results, the highest PEC degradation efficiency and the complete mineralization of BPA on the 90%-{001}TiO_2/CA photoelectrode is attributed to the following facts. First, the {001} facets offer oxidation sites, namely 100% Ti_{5c} atoms that provide the high surface energy. Second, the 90%-{001}TiO_2 shows the highest S_{BET} and $S_{\{001\}BET}$, generating the highest concentration of trapped h⁺ (O^- center), leading to the highest photocurrent density and the biggest total amount of •OH radicals. Third, the photo-generated electrons is rapidly transferred from {001}TiO_2 to CA substrate and further to external circuit under the electric field. The nearly-perfect cube-shaped 90%-{001} TiO_2 is easily to be grown in the porous network of CA, resulting in the efficient separation of electron-hole pairs.

4. Conclusions

In summary, this work studied the dependence of the {001} facet exposure on the PEC degradation of BPA. The fabrication of
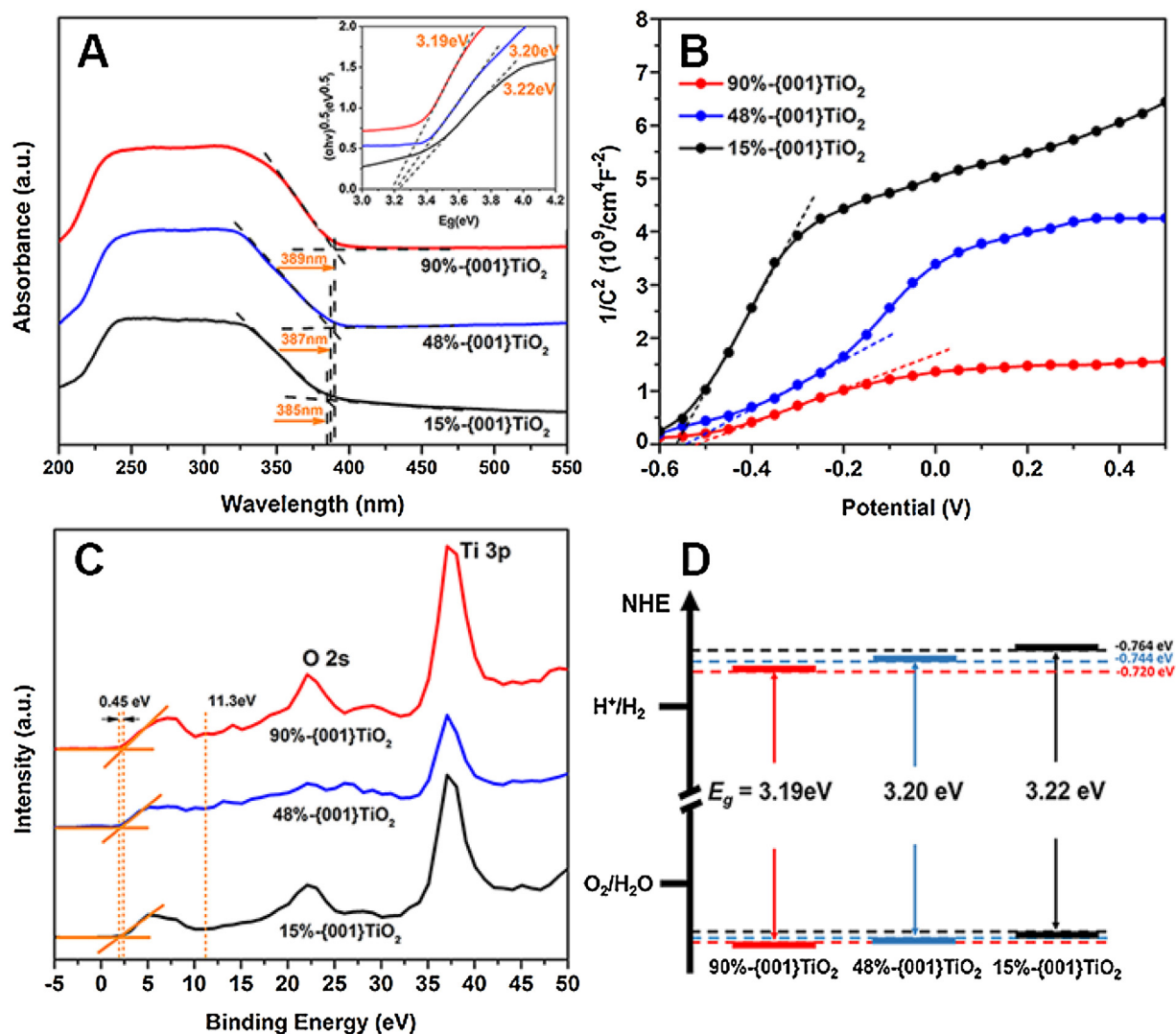
Fig. 7. UV–vis diffuse reflectance absorption spectra (A), Mott−Schottky plots (B), X-ray photoelectron valence-band (VB) spectra (C), determined conduction/and valance bands of three {001}TiO$_2$ samples. The inset in (A) is the transformed Kubelka–Munk function versus the photon energy).
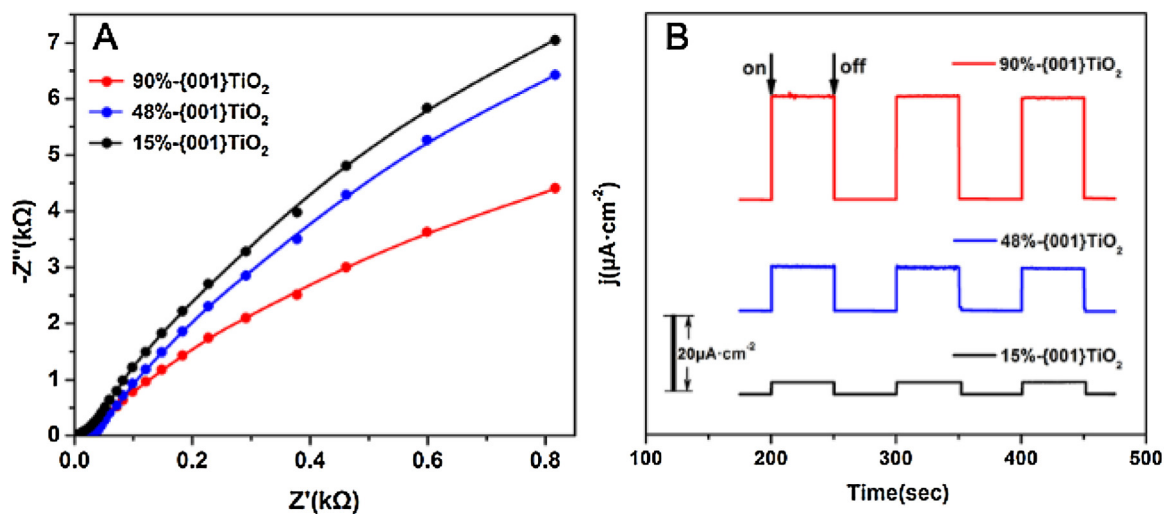

Fig. 8. Nyquist plot of electrochemical impedance spectra (A) and the amperometric i-t curves recorded on three {001}TiO$_2$/CA photoelectrodes. In (B), the curves were recorded in 0.1 M Na$_2$SO$_4$ at a constat voltage of 0.9 V.

three photoelectrodes with varied {001} facet exposure, namely the accurate loading of the facet-controlled nano-sized {001} TiO$_2$ crystal on a CA substrate was conducted via an electrophoretic deposition process. The 90%-{001}TiO$_2$/CA presents the highest photocurrent density towards BPA degradation as well as the highest electron carrier concentration. With a reaction time of 6 h, nearly 100% BPA is removed and a TOC rate of 83% is realized. A positive correlation is suggested between the {001} facet exposure of TiO$_2$ and the PEC oxidation activity. This study provides new insights and valuable original data in the design of highly efficient facet-based TiO$_2$ photoelectrodes and its further environmental PEC applicability in the control of environmental pollution.

Acknowledgments

Appendix A. Supplementary data

Supplementary data associated with this article can be found, in the online version, at http://dx.doi.org/10.1016/j.apcatb.2017.05.042.

References

[1] S. Fukahori, H. Ichiura, T. Kitaoka, H. Tanaka, Appl. Catal. B: Environ. 46 (2003) 453–462.
[2] A.O. Kondrakov, A.N. Ignatev, F.H. Frimmel, S. Bräse, H. Horn, A.I. Revelsky, Appl. Catal. B 160–161 (2014) 106–114.
[3] G. Fent, W.J. Hein, M.J. Moendel, R. Kubiak, Chemosphere 51 (2005) 735–746.
[4] Y.P. Zhang, J.L. Zhou, Chemosphere 73 (2008) 848–853.
[5] S.N. Chai, G.H. Zhao, Y.J. Wang, Y.N. Zhang, Y.B. Wang, Y.F. Jin, X.F. Huang, Appl. Catal. B 147 (2014) 275–286.
[6] D.P. Subagio, M. Srinivasan, M. Lim, T.T. Lim, Appl. Catal. B 95 (2010) 414–422.
[7] C.Y. Wang, H. Zhang, F. Li, L.Y. Zhu, Environ. Sci. Technol. 44 (2010) 6843–6848.
[8] J. Yang, J. Dai, J.T. Li, Environ. Sci. Pollut. Res. 20 (2012) 2435–2447.
[9] O. Bechambi, S. Sayadi, W. Najjar, J. Ind. Eng. Chem. 32 (2015) 201–210.
[10] M. Deborde, S. Rabouan, P. Mazellier, J.P. Duguet, B. Legube, Water Res. 42 (2008) 4299–4308.
[11] Y. Ohko, I. Ando, C. Niwa, T. Tatsuma, T. Yamamura, T. Nakashima, Y. Kubota, A. Fujishima, Environ. Sci. Technol. 35 (2001) 2365–2368.
[12] Y.J. Zhang, G.H. Zhao, Y.N. Zhang, X.F. Huang, Green Chem. 16 (2014) 3860–3869.
[13] G. Liu, H.G. Yang, J. Pan, Y.Q. Yang, G.Q. Lu, H.M. Cheng, Chem. Rev. 114 (2014) 9559–9612.
[14] H. Xu, S.X. Ouyang, L.Q. Liu, P. Reunchan, N. Umezawa, J.H. Ye, J. Mater. Chem. 2 (2014) 12642–12661.
[15] B.C. Qiu, M.Y. Xing, J.L. Zhang, J. Am. Chem. Soc. 136 (2014) 5852–5855.
[16] P.H. Wang, J.Y. Lei, M.Y. Xing, L.Z. Wang, Y.D. Liu, J.L. Zhang, J. Environ. Chem. Eng. 3 (2015) 961–968.
[17] M.Y. Xing, B.X. Yang, H. Yu, B.Z. Tian, S. Bagwasi, J.L. Zhang, X.Q. Gong, J. Phys. Chem. Lett. 4 (2013) 3910–3917.
[18] X.G. Liu, G.J. Dong, S.P. Li, G.X. Lu, Y.P. Bi, J. Am. Chem. Soc. 138 (2016) 2917–2920.
[19] J.G. Wang, Z.F. Bian, J. Zhu, H.X. Li, J. Mater. Chem. A 1 (2013) 1296–1302.
[20] H.M. Wu, J.Z. Ma, Y.B. Li, C.B. Zhang, H. He, Appl. Catal. B 152–153 (2014) 82–87.
[21] Y.N. Zhang, Y.F. Jin, X.F. Huang, H.J. Shi, G.H. Zhao, H.Y. Zhao, Electrochim. Acta 130 (2014) 194–199.
[22] C.-T. Dinh, T.-D. Nguyen, F. Kleitz, T.-O. Do, ACS Nano 3 (2009) 3737–3743.
[23] H. Zong, J. Zhang, G. Shi, Y. Li, Q. Zhang, H. Wang, Electrochim. Acta 179 (2015) 197–205.
[24] M.E. Lindsey, M.A. Tarr, Chemosphere 41 (2000) 409–417.
[25] L. Grinis, S. Dor, A. Ofir, A. Zaban, J. Photochem. Photobiol. A: Chem. 198 (2008) 52–59.
[26] L. Pan, J.J. Zou, S.B. Wang, Z.F. Huang, A. Yu, L. Wang, X.W. Zhang, Chem. Commun. 49 (2013) 6593–6595.
[27] J. Zhu, S.H. Wang, Z.F. Bian, S.H. Xie, C.L. Cai, J.G. Wang, H.G. Yang, H.X. Li, CrystEngComm 12 (2010) 2219–2224.
[28] T.Y. Li, B.Z. Tian, J.L. Zhang, R.F. Dong, T.T. Wang, F. Yang, Ind. Eng. Chem. Res. 52 (2013) 6704–6712.
[29] Y.B. Luan, L.Q. Jing, J. Wu, M.Z. Xie, Y.J. Feng, Appl. Catal. B: Environ. 147 (2014) 29–34.
[30] J.G. Wang, P.H. Rao, W. An, J.L. Xu, Y. Men, Appl. Catal. B 195 (2016) 141–148.
[31] F. Tian, Y.P. Zhang, J. Zhang, C.X. Pan, J. Phys. Chem. C 116 (2012) 7515–7519.
[32] X. Xiao, R. Hao, M. Liang, X.X. Zuo, J.M. Nan, L.S. Li, W.D. Zhang, J. Hazard. Mater 233–234 (2012) 122–130.
[33] Y.H. Lv, Y.Y. Zhu, Y.F. Zhu, J. Phys. Chem. C 117 (2013) 18520–18528.
[34] Y. Hou, X.Y. Li, Q.D. Zhao, G.H. Chen, C.L. Raston, Environ. Sci. Technol. 46 (2012) 4042–4050.
[35] Y.B. Wang, H.Y. Zhao, G.H. Zhao, Appl. Catal. B 164 (2015) 396–406.
[36] J. Pan, G. Liu, G.Q. Lu, H.M. Cheng, Angew. Chem. Int. Ed. 50 (2011) 2133–2137.
[37] W.X. Qi, X.Q. An, F. Zhang, H.J. Liu, J.H. Qu, Appl. Catal. B 206 (2017) 194–202.
[38] H.M. Zhang, X.L. Liu, Y.B. Li, Q.F. Sun, Y. Wang, B.J. Wood, P.R. Liu, D.J. Yang, H.J. Zhao, J. Mater. Chem. 22 (2012) 2465–2472.
[39] X.L. Liu, H.M. Zhang, X.D. Yao, T.C. An, P.R. Liu, Y. Wang, F. Peng, A.R. Carroll, H.J. Zhao, Nano Res. 5 (2012) 762–769.
[40] M.L. Pan, H.J. Zhang, G.D. Gao, L. Liu, W. Chen, Environ. Sci. Technol. 49 (2015) 6240–6248.
[41] L. Yan, J.J. Du, C.Y. Jing, Catal. Sci. Technol. 6 (2016) 2419–2426.
[42] Y.M. Xin, Z.Z. Li, Z.H. Zhang, Chem. Commun. 51 (2015) 15498–15501.
[43] H.Y. Tian, G.H. Zhao, Y.N. Zhang, Y.B. Wang, T.C. Cao, Electrochim. Acta 96 (2013) 199–205.